

ARTICLE OPEN

First-principles screening of structural properties of intermetallic compounds on martensitic transformation

Joohwi Lee^{1,5}, Yuji Ikeda^{1,2} and Isao Tanaka^{1,2,3,4}

Martensitic transformation with good structural compatibility between parent and martensitic phases are required for shape memory alloys (SMAs) in terms of functional stability. In this study, first-principles-based materials screening is systematically performed to investigate the intermetallic compounds with the martensitic phases by focusing on energetic and dynamical stabilities as well as structural compatibility with the parent phase. The B2, D0₃, and L2₁ crystal structures are considered as the parent phases, and the 2H and 6M structures are considered as the martensitic phases. In total, 3384 binary and 3243 ternary alloys with stoichiometric composition ratios are investigated. It is found that 187 alloys survive after the screening. Some of the surviving alloys are constituted by the chemical elements already widely used in SMAs, but other various metallic elements are also found in the surviving alloys. The energetic stability of the surviving alloys is further analyzed by comparison with the data in Materials Project Database (MPD) to examine the alloys whose martensitic structures may cause further phase separation or transition to the other structures.

npj Computational Materials (2017)3:52; doi:10.1038/s41524-017-0053-8

INTRODUCTION

Shape-memory alloys (SMAs) constitute an important class of materials in industrial use because of their shape-memory effect and pseudoelasticity.¹ Already various kinds of SMAs have been well known. Ni–Ti (Nitinol) alloys are now widely used because of its working range around room temperature, good pseudoelastic property, phase stability, and so on.² The Ni–Ti alloys, however, suffer from large thermal hysteresis unless additional elements are included.³ Toxicity of Ni in these alloys is also problematic for bioapplications.⁴ Cu-based SMAs such as Cu–Zn, Cu–Al, and their multicomponent alloys are commercially available because of their low price, but they also have disadvantages, such as instability of martensitic phase, brittleness,⁵ and poor thermo-mechanical performance.⁶ Discovery of new SMAs are therefore still needed for better functional stability,^{7–9} design of working temperature,^{10,11} and other special purposes such as nontoxic biomaterials⁴ and ferromagnetic (FM) SMAs.¹²

To design SMAs, their working temperature and functional stability (reversibility of the shape-memory effect) may be the most important engineering properties. The working temperature is critical particularly to design high-temperature SMAs (HTSMAs). The functional stability is also important to improve the reliability of SMAs. The working temperature is expected to be related to the energetic stability of the martensitic phase relative to that of the parent phase (see the subsection “SMAs reported in experiments”). Meanwhile, some reports have found that better structural compatibility between the parent and the martensitic phases results in smaller thermal hysteresis, which gives better functional stability.^{13,14} We can therefore expect that appropriate energy difference and good structural compatibility between the

parent and the martensitic phases are essential factors when we try to design SMAs.

We can adjust working temperature and functional stability of SMAs by replacing their constituent elements with others. The working temperature of Ni–Ti alloys can be much increased to the range of 400–1200 K by the total or partial replacement of Ni and Ti with the same group elements, namely Pd or Pt^{15,16} and Zr or Hf,¹⁷ respectively. These reports imply that the martensitic phases become energetically more stable than the parent phases at low temperature by replacing constituent elements. Meanwhile, better functional stability, which is associated with smaller thermal hysteresis and functional fatigue can be achieved by adding Cu¹⁴ or Pd¹³ in Ni–Ti alloys and Cr in Ti–Pd alloys.⁹

To discover new materials by modifying their constituent elements, computational research is useful because of its efficiency compared with experimental search. Especially, materials screening based on systematic first-principles calculations prior to experimental synthesis is useful to limit the searching space. Thanks to the recently improved computational machine power, now we can perform systematic first-principles calculations for various combinations of chemical elements with various crystal structures for searching new materials. Indeed, many different materials systems have been investigated in this manner.^{18–21} Hautier et al.¹⁸ and Hinuma et al.¹⁹ have identified new ternary-oxide and zinc-nitride semiconductors, respectively, using the “prototype” crystal structures of Inorganic Crystal Structure Database.²² Carrete et al.²⁰ have reported the semiconductors with the half-Heusler structure that show low thermal conductivity. Greeley et al.²¹ have reported the binary surface alloys to show a good electrocatalytic property.

¹Department of Materials Science and Engineering, Kyoto University, Kyoto 606-8501, Japan; ²Elements Strategy Initiative for Structure Materials (ESISM), Kyoto University, Kyoto 606-8501, Japan; ³Center for Materials Research by Information Integration, National Institute for Materials Science (NIMS), Tsukuba 305-0047 Ibaraki, Japan and ⁴Nanostructures Research Laboratory, Japan Fine Ceramics Center, Nagoya 456-8587 Aichi, Japan

Correspondence: Joohwi Lee (lee.joohwi@gmail.com)

⁵Present address: Toyota Central R&D Laboratories, Inc., Nagakute 480-1192 Aichi, Japan

Received: 17 May 2017 Revised: 21 October 2017 Accepted: 23 October 2017

Published online: 24 November 2017

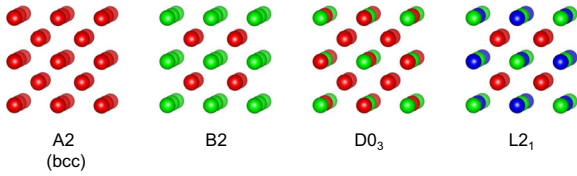


Fig. 1 Crystal structures of the parent phase of the investigated alloys as well as the A2 (bcc) crystal structure. Spheres with different colors are for different chemical elements

There have been theoretical researches on the martensitic transformation by the first-principles calculations. Most of them have been mainly focused on the properties of the specific SMAs, such as the crystal and electronic structures of the martensitic structures,^{23–25} the transformation path and energy profile of the martensitic transformation,^{23,26,27} and the phase diagram obtained by quasi-harmonic approximation.²⁸ However, investigation on various combinations of chemical elements have been rarely reported to the authors' knowledge.

In this study, we perform the first-principles screening to identify intermetallic compounds possessing the energetic and dynamical stabilities of the martensitic phase, as well as the structural compatibility between the parent and the martensitic phases, which is expected to be related to the functional stability. We initially consider 6627 alloys, and 187 survive after the screening. We investigate which elements mainly participate in the surviving alloys. Finally, the energetic stability of surviving alloys are further analyzed by comparison with the first-principles data in Materials Project Database (MPD)²⁹ to examine the alloys which may occur phase separation or transition.

RESULTS AND DISCUSSION

Elements and crystal structures of investigated alloys

We consider binary and ternary alloys with the B2, D0₃, or L2₁ structure as the parent phase at their stoichiometric composition ratios. These parent-phase structures are derived from the body-centered cubic (bcc) structures³⁰ as described in Fig. 1. We investigate combinations of the 48 metallic elements between Li and Bi shown in Fig. 2; specifically, we consider 1128 (=₄₈C₂) XY, 2256 (=₄₈P₂) X₃Y, and 3243 (=3X₄₇C₂) X₂YZ (X=Ti, Cu, Zn) alloys with the B2, D0₃, and L2₁ parent-phase structures, respectively. For the martensitic phases, we consider the orthorhombic 2H (or B19 for the binary alloys with the B2 parent phase) and monoclinic 6M [in the Otsuka notation,^{31,32} which will be used hereafter to correctively refer to 9R (for B2) and 18R (for D0₃ and L2₁) in the Ramsdell notation³³] structures. Both the 2H and 6M martensitic-phase structures have the close-packed basal plane, but they have different stacking orders: “AB” for the 2H structure and “ABCBCACAB” for the 6M structure. Figure 3a shows the crystal structures of the 2H and 6M for ternary X₂YZ alloys with the L2₁ parent phase. The structure of the 2H is explicitly calculated in this study, while the structure of the 6M is estimated from that of the 2H as described later. The space-group type of the 2H structure is *Pmma* for the B2-parent XY alloys and *Pnma* for the D0₃-parent X₃Y and for the L2₁-parent X₂YZ alloys.

The lattice basis for the 2H martensitic structure is given as

$$\mathbf{L}^{2H} = (\mathbf{a}^{2H} \ \mathbf{b}^{2H} \ \mathbf{c}^{2H}) = \begin{pmatrix} a^{2H} & 0 & 0 \\ 0 & b^{2H} & 0 \\ 0 & 0 & c^{2H} \end{pmatrix}, \quad (1)$$

where a^{2H} , b^{2H} , and c^{2H} are the lattice constants of the 2H structure. The unit cell of the parent phase that changes to \mathbf{L}^{2H}

H																	He
Li	Be											B	C	N	O	Fe	Ne
Na	Mg											Al	Si	P	S	Cl	Ar
K	Ca	Sc	Ti	V	Cr	Mn	Fe	Co	Ni	Cu	Zn	Ga	Ge	As	Se	Br	Kr
Rb	Sr	Y	Zr	Nb	Mo	Tc	Ru	Rh	Pd	Ag	Cd	In	Sn	Sb	Te	I	Xe
Cs	Ba	La	Hf	Ta	W	Re	Os	Ir	Pt	Au	Hg	Tl	Pb	Bi	Po	At	Rn

Fig. 2 Periodic table with 48 metallic elements (bold and shaded) focused on in this study

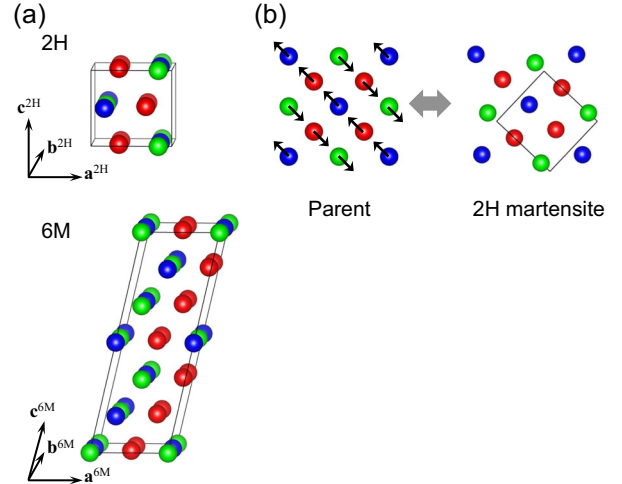


Fig. 3 **a** Crystal structures of the 2H and the 6M martensitic phases for the ternary alloys with the L2₁ parent phase. **b** Transformation between the parent and the martensitic phases. Small black arrows on spheres denote the atomic movement, and the rectangle denotes the unit cell of the 2H crystal structure

after the martensitic transformation may be given as

$$\mathbf{L}^{p \rightarrow 2H} = \begin{pmatrix} \mathbf{a}^p - \mathbf{b}^p & -\mathbf{c}^p & \mathbf{a}^p + \mathbf{b}^p \\ a^p & 0 & a^p \\ -a^p & 0 & a^p \\ 0 & -a^p & 0 \end{pmatrix} \quad (\text{for B2}) \quad (2)$$

and

$$\mathbf{L}^{p \rightarrow 2H} = \begin{pmatrix} (\mathbf{a}^p - \mathbf{b}^p)/2 & -\mathbf{c}^p & (\mathbf{a}^p + \mathbf{b}^p)/2 \\ a^p/2 & 0 & a^p/2 \\ -a^p/2 & 0 & a^p/2 \\ 0 & -a^p & 0 \end{pmatrix} \quad (\text{for D0}_3 \text{ and L2}_1), \quad (3)$$

where \mathbf{a}^p , \mathbf{b}^p , and \mathbf{c}^p are the lattice basis of the conventional unit cell for the parent phase structures, and a^p is their lattice constant. The deformation gradient³⁴ \mathbf{F}^{2H} is then obtained as

$$\mathbf{F}^{2H} = \mathbf{L}^{2H} (\mathbf{L}^{p \rightarrow 2H})^{-1}. \quad (4)$$

Figure 3b describes the martensitic transformation between the L2₁ parent and its 2H martensitic phases. It should be emphasized that the martensitic transformation path is similar to the Burgers path^{35,36} for pure metals, which describes the transformation between the bcc and the hexagonal close-packed structures.

In order to reduce computational costs, the crystal structure of the 6M is estimated from that of the 2H as follows. We first assume that their basal-plane structure and layer distance along the stacking direction are the same for both the 2H and 6M. We further assume that the stacking position of each layer is different exactly by $a^{2H}/3$ along \mathbf{a}^{2H} . Then, the lattice basis for the 6M

structure is given as

$$\mathbf{L}^{6M} = (\mathbf{a}^{6M} \mathbf{b}^{6M} \mathbf{c}^{6M}) = \begin{pmatrix} a^{2H} & 0 & -a^{2H}/3 \\ 0 & b^{2H} & 0 \\ 0 & 0 & 3c^{2H} \end{pmatrix}. \quad (5)$$

The unit cell of the parent phase that changes to the \mathbf{L}^{6M} after the martensitic transformation may be given as

$$\mathbf{L}^{p \rightarrow 6M} = (\mathbf{a}^p - \mathbf{b}^p \quad -\mathbf{c}^p \quad 3(\mathbf{a}^p + \mathbf{b}^p)) = \begin{pmatrix} a^p & 0 & 3a^p \\ -a^p & 0 & 3a^p \\ 0 & -a^p & 0 \end{pmatrix} \quad (\text{for } B2) \quad (6)$$

and

$$\mathbf{L}^{p \rightarrow 6M} = ((\mathbf{a}^p - \mathbf{b}^p)/2 \quad \mathbf{c}^p \quad 3(\mathbf{a}^p + \mathbf{b}^p)/2) = \begin{pmatrix} a^p/2 & 0 & 3a^p/2 \\ -a^p/2 & 0 & 3a^p/2 \\ 0 & -a^p & 0 \end{pmatrix} \quad (\text{for } DO_3 \text{ and } L2_1). \quad (7)$$

The deformation gradient \mathbf{F}^{6M} is then obtained as

$$\mathbf{F}^{6M} = \mathbf{L}^{6M}(\mathbf{L}^{p \rightarrow 6M})^{-1}. \quad (8)$$

Materials-screening conditions

Figure 4 shows the flowchart of the materials screening.

Firstly, we check whether or not the space-group type of the optimized structure of the 2H martensitic phase ($\mathbf{G}_{\text{opt}}^m$) is the same as the expected one ($\mathbf{G}_{\text{init}}^m$). For many investigated alloys, the 2H structure is optimized to the parent-phase structure or to some other structures. Such alloys are excluded from the screening because they cannot have the assumed martensitic structure. The space-group types of the optimized structures are checked using the SPGLIB library inside the PHONOPY code.^{37,38}

Secondly, we investigate the energetic stability. Here we check whether the energy of the martensitic phase (E^m) is smaller than that of the parent phase (E^p). Only the alloys satisfying $\Delta E^{m-p} \equiv E^m - E^p < 0$ survive. We also guarantee that the 2H martensitic phase is energetically more stable than pure metals as references. Here, the formation energy of the martensitic phase relative to those of pure metals in their most stable crystal structures, E_f^m , must be smaller than zero.

Thirdly, the structural compatibility between the parent and the martensitic phases is considered. For this purpose, we use the transformation stretch tensors³⁴ \mathbf{U}^{2H} and \mathbf{U}^{6M} , which are positive-definite and symmetric matrices. These matrices are obtained from \mathbf{F}^{2H} and \mathbf{F}^{6M} using the polar decomposition as

$$\mathbf{F}^{2H} = \mathbf{R}^{2H} \mathbf{U}^{2H} \quad (9)$$

and

$$\mathbf{F}^{6M} = \mathbf{R}^{6M} \mathbf{U}^{6M}, \quad (10)$$

where \mathbf{R}^{2H} and \mathbf{R}^{6M} are rotation matrices. James et al. have shown using their model that when the second largest eigenvalue λ_2 of \mathbf{U} (hereafter the \mathbf{U}^{2H} or \mathbf{U}^{6M} are collectively referred to as \mathbf{U}) is equal to one, the two phases can make a distortionless interface,³⁴ which is intuitively expected as an advantage for showing better functional stability. Indeed, several SMAs with small thermal hysteresis and functional fatigue are found by modifying the composition ratios to realize λ_2 close to one.^{8,9,13,39} Based on these reports, we adopt $|\lambda_2 - 1| < 0.01$ as a screening condition. We also consider the volume difference between the parent and the martensitic phases, because the large volume difference is expected to cause huge stress between the two phases and to result in low functional stability.³⁹ Actually, several materials

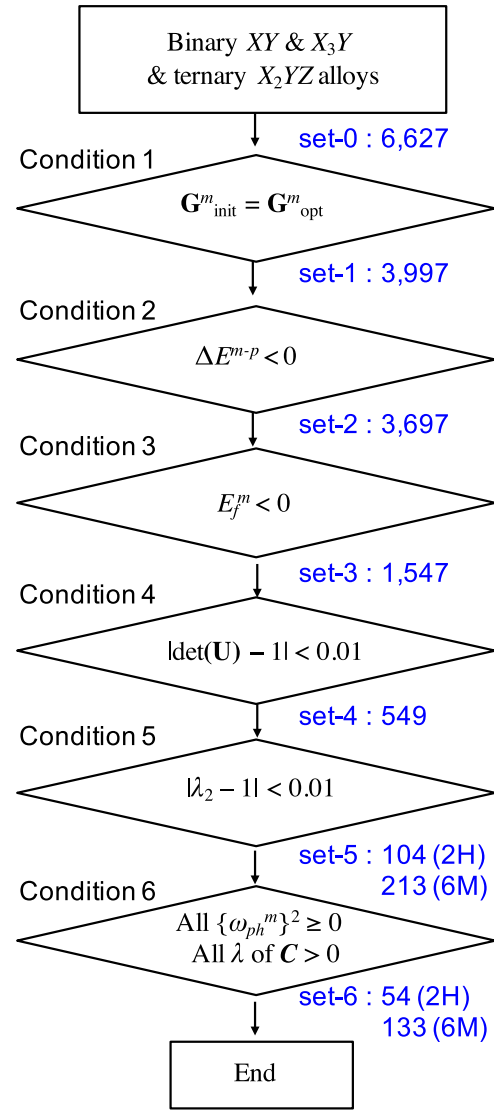


Fig. 4 Flowchart of the materials screening. The number of surviving alloys at each step is shown in blue. Conditions 1–3, 4–5, and 6 are related to the energetic stability of the martensitic phase, the structural compatibility between parent and martensitic phases, and the dynamical stability of the martensitic phase, respectively. The lists of 187 surviving alloys with the 2H and 6M martensitic structures are given in Tables 2 and 3

systems such as lithium-ion batteries, whose applications are related to their phase transitions, are known to have good advantage of reliability when they show small volume differences.⁴⁰ The relative difference between the volume of the parent (V^p) and the martensitic (V^m) phases are obtained as $\det(\mathbf{U})$, and hence we adopt $|\det(\mathbf{U}) - 1| < 0.01$ as another screening condition.

Lastly, the dynamical stability of the martensitic phase is investigated. For this purpose, we analyze the phonon frequencies of the martensitic phases ω_{ph}^m and elastic modulus matrix (\mathbf{C}) of the martensitic phases. The alloys with imaginary phonon frequencies, i.e., $\{\omega_{ph}^m\}^2 < 0$ for some phonon modes, are screened out, because the existence of the imaginary phonon frequencies indicates that the crystal structure is dynamically unstable. Phonon dispersion curves and density of states are used to confirm the dynamical stability of martensitic phase by the existence of the imaginary phonon frequencies. We also screen

Table 1. Characteristic martensitic transformation temperatures for 13 experimentally reported SMAs with nearly stoichiometric composition ratios. The data correspond to those in Fig. 5

This study		Experimental reports						
Calculated composition	ΔE^{m-p} (eV/atom)	Experimental composition	M_s (K)	M_f (K)	A_s (K)	A_f (K)	T_c (K)	Ref.
AgCd ^a	-0.005	Ag ₅₁ Cd ₄₉					~223	43
AuCd	-0.005	Au ₅₀ Cd ₅₀	~293	~323			~308	42
TiAu	-0.078	Ti ₅₀ Au ₅₀	834	823	852	861	843	15
Zn ₂ AuCu	-0.012	Zn ₄₅ Au ₃₀ Cu ₂₅	235	233	235	237	235	8
Co ₂ NiGa	-0.042	Co ₅₀ Ni ₂₄ Ga ₂₆	~323	~348			~336	44
Ti ₃ Nb	-0.024	Ti ₇₆ Nb ₂₄	~338				~338	45
Ni ₂ MnGa	-0.006	Ni ₅₀ Mn ₂₅ Ga ₂₅	275		281		278	12
TiNi	-0.043	Ti ₅₀ Ni ₅₀	218	240	269	280	252	15
TiPd ^b	-0.082	Ti ₅₀ Pd ₅₀	783	717	757	787	761	15
TiPt ^b	-0.155	Ti ₅₀ Pt ₅₀	1307	1257	1277	1322	1291	15
Ti ₂ NiPd ^b	-0.067	Ti _{50.5} Ni _{24.5} Pd ₂₅	452	440	457	468	454	16
Ti ₂ NiPt ^b	-0.087	Ti _{50.5} Ni _{24.5} Pt ₂₅		663		778	721	46
Ti ₂ PtIr ^b	-0.120	Ti ₅₀ Pt ₂₅ Ir ₂₅	1383	1341	1394	1463	1395	47

^a Detailed characteristic temperatures are not reported in ref. 43

^b The energy of the B19' structure is slightly lower than that of the B19 structure, which is reported to exist in experiments but dynamically unstable for 0 K first-principles simulations. In this study, ΔE^{m-p} is calculated using B19' as the martensitic-phase structure

out the alloys whose elastic modulus matrices are not positive definite according to Born's elastic stability criteria.⁴¹ Note that the dynamical stability of the 6M martensitic structure is assumed to be the same as that of the 2H martensitic structure.

SMAs reported in experiments

Prior to the materials screening, we first investigate ΔE^{m-p} for 13 alloys that were reported to show the shape-memory effect near the stoichiometric composition ratios in experiments. Table 1 summarizes the experimental transformation temperature T_c and the computed ΔE^{m-p} for the 13 SMAs, and Fig. 5 shows their correlation. Here T_c is determined as the average over the reported characteristic martensitic transformation temperatures A_s , A_f , M_s , and M_f in experiments.^{8,12,15,16,42-47} When some SMAs were reported to have different martensitic structures from 2H in experiments or theoretical calculations, the energies of these crystal structures are additionally calculated to obtain ΔE^{m-p} . Among 13 alloys, Ni₂MnGa and Co₂NiGa are known as the FM alloys with the Curie temperatures of 376 K⁴⁸ and 377 K,⁴⁹ respectively. The experimental martensitic transformation temperatures of these alloys are below their Curie temperatures. Our calculations confirm that both the parent-phase and the martensitic-phase structures of these two alloys are more than 0.04 eV/atom energetically more stable in the FM state than in the NM state.

We can derive three results from the obtained data. Firstly, the martensitic phases have lower energies than the parent phase for all the 13 investigated SMAs. Since the first-principles calculations give the energies at 0 K, this result supports the experimental fact that the martensitic phases are found at lower temperature than the parent phase for the 13 SMAs. Secondly, most of the energy differences among various martensitic phases are less than 0.01 eV/atom, which are much smaller than the energy differences between the parent and the martensitic phases. This guarantees that the energy of the 2H structure can be used as the representative value among the various martensitic phases for the screening procedure using ΔE^{m-p} . Thirdly, the computed ΔE^{m-p} shows strong correlation with the experimental T_c . Specifically, the SMAs with large $|\Delta E^{m-p}|$ show high T_c . The linear correlation coefficient between ΔE^{m-p} and T_c is -0.92. This implies that ΔE^{m-p}

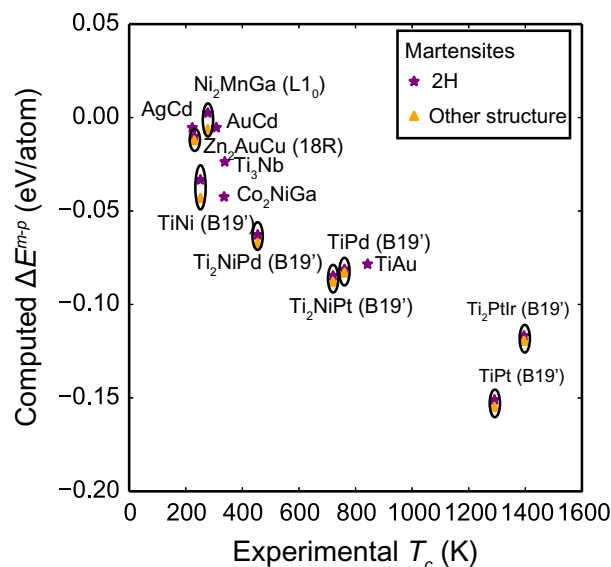


Fig. 5 Relationship of computed ΔE^{m-p} and experimental transformation temperature T_c of 13 SMAs near the stoichiometric composition ratios in experiments. In addition to the 2H structure (star purple symbols), martensitic-phase structures in the parentheses (triangle orange symbols), which are reported in experiments or simulations, are also investigated. The computed ΔE^{m-p} and experimental T_c show strong correlation with the linear correlation coefficient (r) of -0.92

ΔE^{m-p} can be used to roughly but efficiently estimate T_c for various kinds of alloys. For example, the ΔE^{m-p} of -0.05 eV/atom corresponds to T_c of 400 K.

Figures 6 and 7 show the phonon dispersion curves of parent and martensitic phases, respectively, for the 13 SMAs. For the martensitic phases, we investigate energetically the most stable crystal structure for each of the 13 SMAs. These martensitic structures do not show any imaginary modes, indicating that they are dynamically stable. These martensitic structures also show the

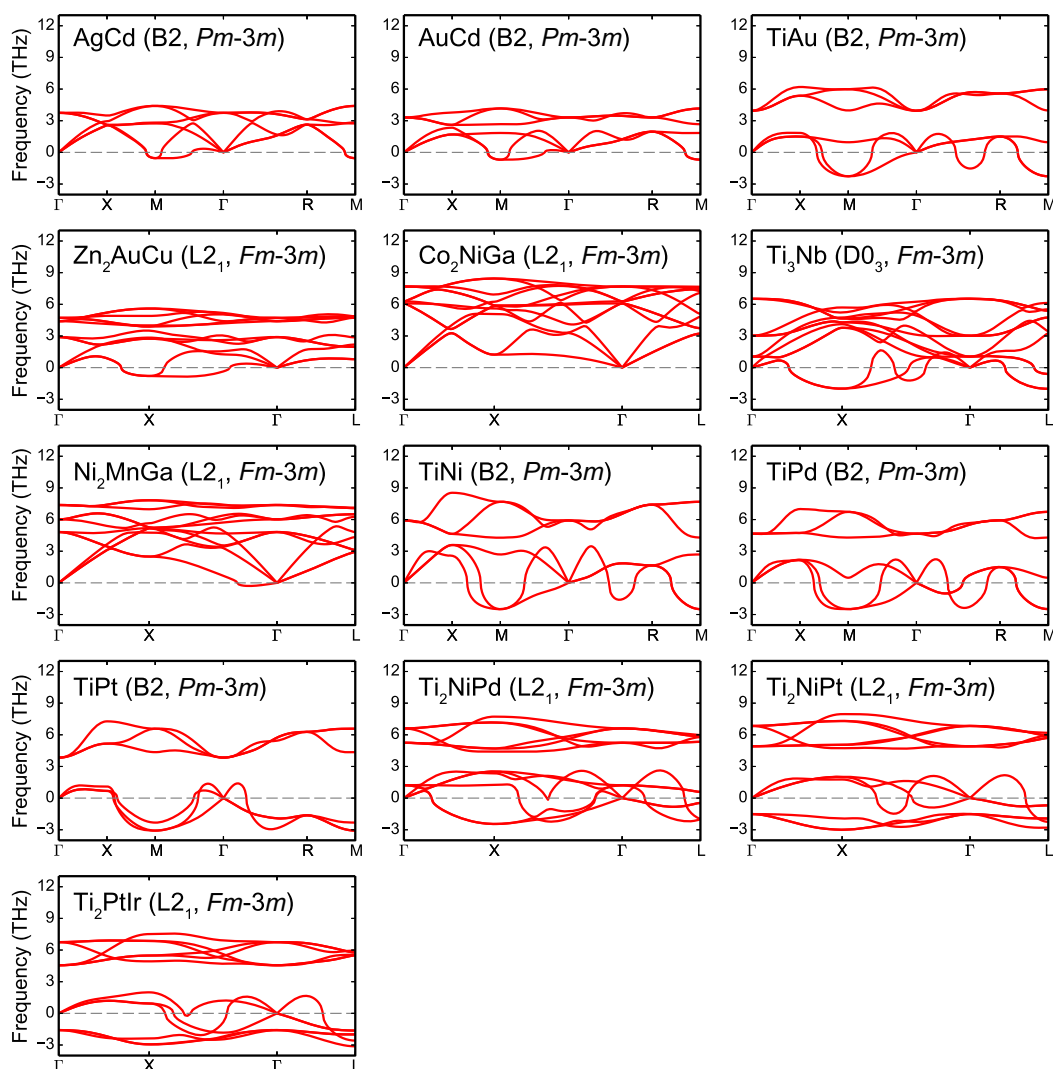


Fig. 6 Phonon dispersion curves for the parent-phase structures of the 13 SMAs with stoichiometric composition ratios. The space-group type of the structure is also shown in each panel. The band paths in the Brillouin zones are set based on the space-group type of the structure.⁷⁵ Most of the parent phases of 13 SMAs show imaginary modes

elastic stability confirmed by the positive definite elastic modulus matrices. This satisfies our screening condition that the martensitic structures should be dynamically stable. In contrast, the parent phases of the most of the 13 SMAs show imaginary frequencies in a wide range of wave vectors. This indicates that they are dynamically unstable under the harmonic approximation. The anharmonic phonon effects,^{50,51} which is significant particularly at high temperature, is probably essential to make the parent phases dynamically stable.

According to these results, we expect that the screening conditions for the energetic and dynamical stabilities described in subsection “Materials-screening conditions” are suitable to find intermetallic compounds which possibly cause a martensitic transformation. Later we will also discuss the structural compatibility of the 13 investigated alloys.

Energetic and structural properties of the martensitic phase of intermetallic compounds

In order to identify the intermetallic compounds whose martensitic phase is energetically and dynamically stable and shows good structural compatibility with the parent phase, we apply the screening conditions described in subsection “Materials-screening

conditions” and Fig. 4 to 6627 alloys. Figure 8 shows the correlations among four quantities, ΔE^{m-p} , E_f^m , $\det(\mathbf{U}) - 1$, and $\lambda_2 - 1$, for 3997 alloys in the set-1. Gaussian kernel density estimation⁵² is used to put colors in the plots. There are no strong correlations among the four quantities. The maximum magnitude of the linear correlation coefficient is only 0.42, found between ΔE^{m-p} and $\det(\mathbf{U}) - 1$. This indicates that these four screening conditions work almost independently. The screening conditions are also indicated in Fig. 8 as gray vertical and horizontal lines. Although our screening conditions are rather tight especially for $\det(\mathbf{U}) - 1$ and $\lambda_2 - 1$, as many as 187 alloys survive because of the high density of alloys within the screening-condition slot. The lists of surviving alloys with the 2H and 6M martensitic structures are given in Tables 2 and 3, respectively. Among 187 alloys, 54 and 133 alloys correspond to the 2H and 6M martensitic structures, respectively. The surviving alloys tend to have the 6M martensitic structure more than the 2H.

It is interesting that the 13 SMAs analyzed in previous subsection are not included in the list of surviving alloys. We confirm that they satisfy the screening condition for the energetic and dynamical stability of the martensitic phase. However, they do not satisfy the remaining two screening conditions related to the structural compatibility ($|\lambda_2 - 1| < 0.01$ and $|\det(\mathbf{U}) - 1| < 0.01$).

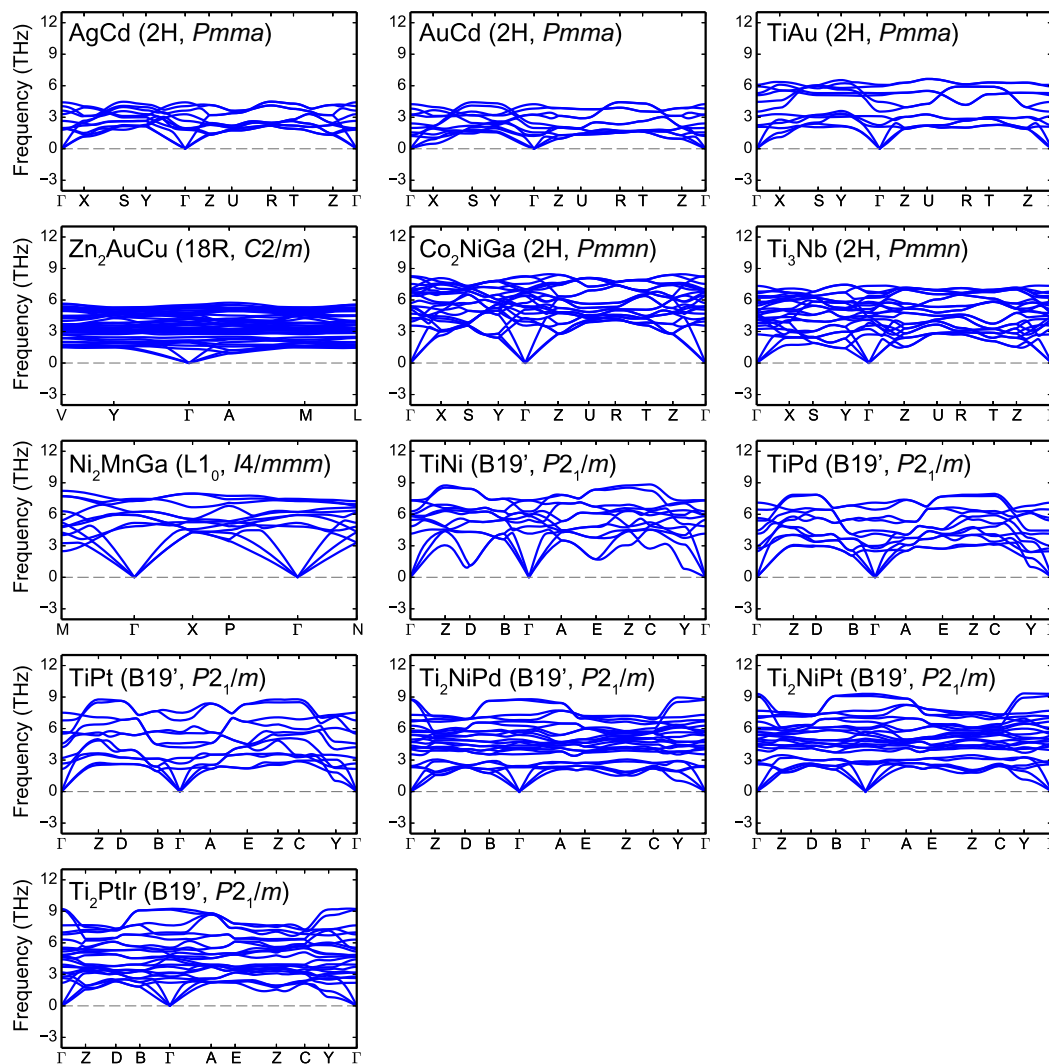


Fig. 7 Phonon dispersion curves for the martensitic-phase structures of the 13 SMAs with stoichiometric composition ratios. The space-group type of the structure is also shown in each panel. The band paths in the Brillouin zones are set based on the space-group type of the structure.⁷⁵ All of the martensitic phases of 13 SMAs do not show any imaginary modes

Their low structural compatibility implies their low functional reliability. Actually, the experimental reports (Table 1) show that the thermal hysteresis of these alloys, except for Zn_2AuCu , is larger than 20–30 K, which is not small.^{3,53} The larger thermal hysteresis should result in the worse functional stability. It is worth referring to the experimental reports that some of these alloys reduce their thermal hysteresis by deviating their composition ratios from the stoichiometric and/or adding dopant elements; Zn–Au–Cu shows low thermal hysteresis of ~2 K by adjusting its composition ratio,⁸ Ti–Ni reduces the thermal hysteresis by doping Pd, Pt, Cu, or Au,^{3,13,14} and Ti–Pd achieves less than 5 K of thermal hysteresis by doping Cr.⁹ These reports indicate the possibility to control the functional stability of SMAs by introducing nonstoichiometric composition ratios and/or dopant elements.

Figure 9 shows the chemical combinations of 111 surviving binary alloys. The ternary X_2YZ alloys are excluded for this analysis because in this study the X component for the ternary is restricted to three elements, i.e., Ti, Cu, and Zn.

The alloys composed of the elements from the same combination of groups tend to have the same type of martensitic structures. Two or more X_3Y alloys survive in 24 group-combinations, and among them, 20 combinations have the same

type of martensitic structures. This tendency may be related to the same number of valence electrons of the alloys formed by chemical elements in the same combinations of groups in the periodic table.

All the surviving ten XY alloys include at least one chemical element in the groups 10–13. Among 101 combinations of X_3Y alloys, 28 alloys are only composed of the chemical elements in the groups 10–12. Other 15 alloys are formed by the combinations of a chemical element in the group 3 or 4 as X and the other one in the groups 10–14 as Y . Thus, almost half of the surviving binary alloys (53 out of 111) include some chemical elements in the groups 10–14. On the other hand, the other 58 surviving X_3Y binary alloys are found in various combinations of groups. It is therefore difficult to categorize them into some specific combinations of the groups in the periodic table.

Hence, next the surviving binary alloys are analyzed from the element-resolved viewpoint. Among the 48 chemical elements, Cu, Zn, Ag, Au, and Pd are the most frequently included elements in the descending order. The result is reasonable since many Cu-based alloys are known to exhibit the shape-memory effects. Cu–Zn-based SMAs are found in the form of either binary alloys of 60–64 at.% Cu⁵⁴ or ternary alloys incorporating Al, Si, Ga, and Mn.⁵

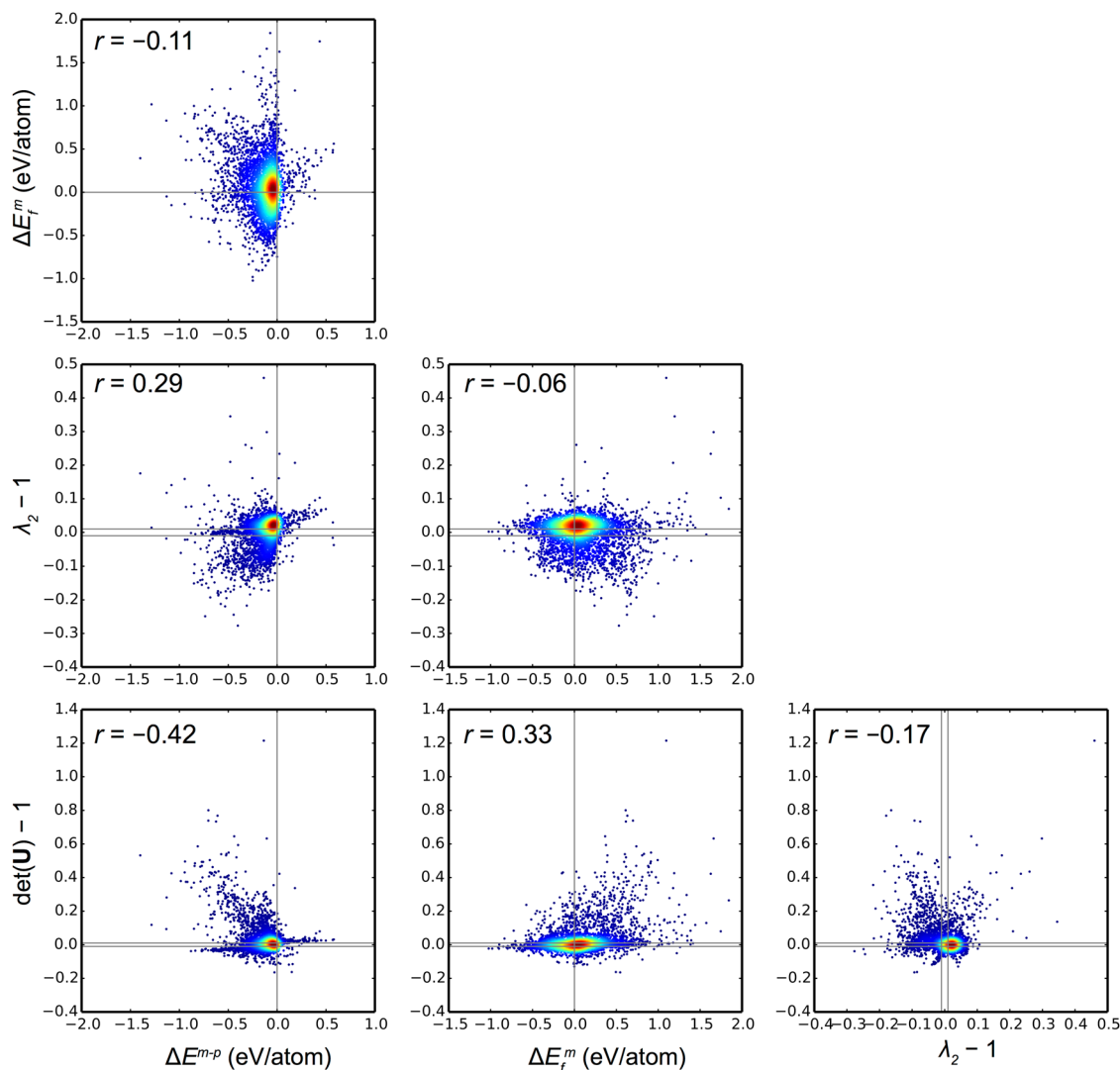


Fig. 8 Scatter plots between the quantities associated with the screening conditions for 3997 alloys in the set-1 in Fig. 4. The gray lines denote the boundary of screening-condition slot. The color scale represents the relative density of points generated by Gaussian kernel density estimation. Blue and red colors correspond to higher and lower densities, respectively. r shown in each panel is the linear correlation coefficient. There are no strong correlations among the four quantities, which indicates that these four screening conditions work almost independently

Cu–Al-based SMAs are found in the form of ternary alloys incorporating Ni,⁵⁵ Mn,⁵⁶ Be,⁵⁷ and Zn.⁵ Cu–Sn-based binary alloys also show the shape-memory effect for 74–91 at.% Cu.⁵ Note that these alloys are not included in the 13 SMAs analyzed in previous subsection because their shape-memory effect were reported in experiments only for the off-stoichiometric composition ratios.

Besides these popular alloy systems, many other elements and their combinations are found in the surviving alloys. Among such elements, Li and Sc have been rarely used as the constituent elements of the SMAs reported in experiments. Only recently, the Mg₈₀Sc₂₀ alloy was discovered as a SMA having technological advantages with its light weight.⁵⁸ The In–Ti nanowire was also reported to exhibit the shape-memory effect.⁵⁹ These reports support that it is possible to make the alloys which cause a martensitic transformation from the less popular elements.

According to several review papers,^{10,11} the SMAs with the T_c above 370–400 K are categorized in HTSMAs. Since the ΔE^{m-p} of -0.05 eV/atom approximately corresponds to the T_c of 400 K as described in previous subsection, it may be interesting to classify the surviving alloys at $\Delta E^{m-p} = -0.05$ eV/atom. Among the 111 surviving binary alloys, 60 alloys show $\Delta E^{m-p} < -0.05$ eV/

atom, which are shown in blue in Fig. 9. Al, Sc, Ti, Zn, Hf, and Pt are found five or more times in the surviving alloys with $\Delta E^{m-p} < -0.05$ eV/atom. These chemical elements, except for Zn, are not so much included in the alloys with -0.05 eV/atom $< \Delta E^{m-p} < 0$. This indicates that these elements are preferable to show T_c over ~ 400 K. Indeed, Pt-rich alloys such as Pt–Al and Pt–Ga⁶⁰ are used for HTSMAs.

Finally, energetic stability of the 187 surviving alloys is examined. The stability is already examined by the formation energy E_f^m with respect to pure metals as described in the subsection “Materials-screening conditions”. Besides E_f^m , the energy of the alloys can be compared with the convex-hull energy for the corresponding binary and ternary systems. Since the construction of the convex-hull energy for many systems is computationally laborious, we refer to the data of the MPD,²⁹ which were obtained under similar computational conditions with the present study. The convex-hull energy of the corresponding chemical composition relative to pure metals in MPD, $E_f^{\text{conv}}(\text{MPD})$, is compared to the present E_f^m . Tables 2 and 3 show the difference $E_f^m - E_f^{\text{conv}}(\text{MPD})$, together with the corresponding phases for the given composition. Most of the 2H and 6M structures for the

Table 2. Surviving 54 alloys with the 2H martensitic structure after the materials screening

	Alloy	This study			Data from MPD ²⁹	Difference	
		Magnetic moment ($\mu\text{B}/\text{atom}$) ^a	ΔE^{m-p} (eV/atom)	E_t^m (eV/atom)	Reported convex hull ^b	$E_t^m - E_t^{\text{conv}}(\text{MPD})$ (eV/atom)	
XY	NaTi		-0.013	-0.126	NaTi (<i>Fd-3m</i>)	-0.010	
X_3Y	Tl ₃ Bi		0.000	-0.029	Tl ₃ Bi (<i>P6₃/mmc</i>)	-0.002	
	Tl ₃ Na		-0.018	-0.088	Tl ₃ Na (<i>Pm-3m</i>)	-0.005	
	Tl ₃ Ca		-0.018	-0.224	Tl ₃ Ca (<i>Pm-3m</i>)	0.019	
	Au ₃ In		-0.038	-0.136	Au ₃ In (<i>Fm-3m</i>)	-0.038	
	Mg ₃ Zn		-0.041	-0.037	Mg + Mg ₂₁ Zn ₂₅	0.020	
	Zn ₃ Cu		-0.053	-0.075	Zn ₈ Cu ₅ + Zn	-0.010	
	Cd ₃ Ag		-0.053	-0.045	Cd ₈ Ag ₅ + Cd	-0.004	
	Cd ₃ Pt		-0.054	-0.199	CdPt + Cd	-0.037	
	Cu ₃ Sn		-0.057	-0.002	Cu + CuSn	0.012	
	Zn ₃ Ag		-0.058	-0.045	Zn ₈ Ag ₅ + Zn	-0.014	
	Zn ₃ Co		-0.059	-0.041	Zn ₁₃ Co + Co	-0.001	
	Cd ₃ Rh		-0.061	-0.087	Cd + Rh	-0.087	
	Zn ₃ Au		-0.070	-0.159	Zn ₃ Au (<i>Pm-3n</i>)	-0.005	
	Be ₃ Pt		-0.080	-0.477	Be ₁₂ Pt + Pt	-0.393	
	Zn ₃ Rh		-0.082	-0.313	Zn ₃ Rh (<i>P6₃/mmc</i>)	0.016	
	Sc ₃ In	0.30 (P) 0.05 (M)	-0.093	-0.258	Sc ₃ In (<i>P6₃/mmc</i>)	0.047	
	Sc ₃ Al	0.50 (P) 0.00 (M)	-0.094	-0.247	Sc ₃ Al (<i>Pm-3m</i>)	0.022	
	Pd ₃ Y		-0.096	-0.796	Pd ₃ Y (<i>Pm-3m</i>)	0.070	
	Zn ₃ Ir		-0.099	-0.219	Zn ₃ Ir (<i>I4/mmm</i>)	-0.004	
	Zn ₃ Ru		-0.100	-0.088	Zn ₃ Ru (<i>I4/mmm</i>)	0.051	
	Sc ₃ Tl	0.43 (P) 0.02 (M)	-0.120	-0.187	Sc + Tl	-0.187	
	Ru ₃ Sc	0.50 (P) 0.00 (M)	-0.130	-0.086	Ru + ScRu ₂	0.210	
	Sc ₃ Zr		-0.136	-0.007	Sc + Zr	-0.007	
	Sc ₃ Sn	0.37 (P) 0.00 (M)	-0.151	-0.436	Sc + Sc ₅ Sn ₃	0.020	
	Sc ₃ Pb	0.45 (P) 0.00 (M)	-0.163	-0.271	Sc + Sc ₅ Pb ₃	0.045	
	Rh ₃ Y	0.42 (P) 0.00 (M)	-0.181	-0.405	Rh + Rh ₂ Y	0.151	
	Hf ₃ Sc		-0.208	-0.004	Sc + Hf ₅ Sc	0.008	
	Os ₃ Ti		-0.333	-0.136	TiOs + Os	0.221	
	Os ₃ Hf		-0.352	-0.108	HfOs + Os	0.247	
	Os ₃ Zr		-0.370	-0.040	ZrOs ₂ + Os	0.254	
	Zn_2YZ	Zn ₂ ScCr	0.94 (P) 0.93 (M)	-0.003	-0.088	Cr + ScZn ₂	0.082
		Zn ₂ CrZr	0.83 (P) 0.77 (M)	-0.007	-0.022	Cr + ZrZn ₂	0.125
		Zn ₂ LiGa		-0.029	-0.176	LiZn ₃ + LiGa ₃	-0.009
Zn ₂ BeNi			-0.053	-0.126	BeNi + Be ₃ Ni + Zn ₁₁ Ni ₂	0.114	
Zn ₂ MgAg			-0.057	-0.127	Mg ₂ Zn ₁₁ + MgZn ₂ + MgZnAg ₂	0.003	
Zn ₂ AlNi			-0.142	-0.246	Zn + Zn ₁₁ Ni ₂ + Al ₄ Ni ₃	0.085	
Zn ₂ AlCo			-0.164	-0.160	Zn + AlCo	0.082	
Zn ₂ CoGa			-0.186	-0.080	Zn + GaCo + Ga ₃ Co	0.060	
Cu_2YZ	Cu ₂ InAu		-0.017	-0.073	Cu + Cu ₃ Au + In ₂ Au	0.037	
	Cu ₂ ZnGa		-0.021	-0.101	Zn ₈ Cu ₅ + GaCu ₃ + Ga ₂ Cu	-0.004	
	Cu ₂ AlAg		-0.026	-0.097	Al + AlCu + Al ₄ Cu ₉	0.062	
	Cu ₂ GaAg		-0.028	-0.036	Ag + GaCu ₃ + GaAg ₂	0.041	
	Cu ₂ LiSb		-0.040	-0.189	Cu + Sb + Li ₂ Sb	0.024	
	Cu ₂ GaAu		-0.054	-0.140	GaCu ₃ + Cu ₃ Au + GaAu	-0.020	
	Cu ₂ PdSn		-0.064	-0.203	Cu + SnPd + Sn ₂ Pd	0.066	
	Cu ₂ NiSn		-0.093	-0.061	Cu + Ni ₃ Sn ₂ + Ni ₃ Sn ₄	0.058	
	Cu ₂ SnPt		-0.096	-0.198	Cu + SnPt + Sn ₃ Pt ₂	0.095	
	Cu ₂ AlRu		-0.105	-0.123	Cu + AlRu + Al ₂ Ru	0.224	
	Cu ₂ GaPt		-0.112	-0.322	Cu + GaCuPt ₂ + Ga ₃ Pt ₂	-0.015	
Ti_2YZ	Ti ₂ AuTi	0.42 (P) 0.58 (M)	-0.064	-0.109	Ti ₃ Au + TiAu + Ti	0.172	
	Ti ₂ CdPt	0.25 (P) 0.44 (M)	-0.082	-0.367	TiPt + Ti ₃ Pt + Cd	0.191	
	Ti ₂ PbPd	0.40 (P) 0.55 (M)	-0.084	-0.211	Ti ₃ Pb + Ti ₂ Pd + Pb	0.129	
	Ti ₂ InAu	0.37 (P) 0.55 (M)	-0.094	-0.257	Ti ₃ Au + In + In ₂ Au	0.037	

^a Magnetic moments in the ferromagnetic state are shown. P and M denote the magnetic moments of the parent-phase and the martensitic-phase structures, respectively

^b The symbol in the parentheses for the single phase indicates its space-group type

Table 3. Surviving 133 alloys with the 6M martensitic structure after the materials screening

	Alloy	This study			Data from MPD ²⁹	Difference
		Magnetic moment (μB/atom) ^a	ΔE^{m-p} (eV/atom)	E_f^m (eV/atom)	Reported convex hull ^b	$E_f^m - E_f^{\text{conv}}(\text{MPD})$ (eV/atom)
XY	MgIn		-0.005	-0.062	MgIn (<i>P4/mmm</i>)	-0.008
	ZrCd		-0.007	-0.081	Zr + ZrCd ₃	-0.009
	PdAg		-0.029	-0.032	Pd + PdAg ₃	0.004
	AgAu		-0.033	-0.052	Ag + AgAu ₃	-0.031
	AlCu		-0.040	-0.183	AlCu (<i>P2/m</i>)	0.030
	AlAg		-0.074	-0.031	Al + AlAg ₃	0.022
	TiAl		-0.100	-0.354	TiAl (<i>P4/mmm</i>)	0.049
	InHf		-0.112	-0.049	In ₅ Hf ₂ + Hf	0.058
	NiRe		-0.356	-0.024	Ni + NiRe ₃	0.050
	X ₃ Y	Li ₃ Cd		-0.001	-0.185	Li ₃ Cd (<i>I4/mmm</i>)
Co ₃ Ga		1.02 (P) 1.00 (M)	-0.002	-0.102	Co + CoGa	0.037
Li ₃ Hg			-0.002	-0.287	Li ₃ Hg (<i>Fm-3m</i>)	-0.009
Li ₃ Zn			-0.003	-0.108	Li + LiZn	-0.002
Li ₃ Ag			-0.003	-0.161	Li ₃ Ag (<i>I4/mmm</i>)	-0.001
Na ₃ In			-0.003	-0.060	Na + Na ₂ In	0.030
Na ₃ Tl			-0.003	-0.089	Na ₃ Tl (<i>Pm-3m</i>)	-0.006
Li ₃ Rh			-0.004	-0.042	Li + LiRh	0.056
Li ₃ Au			-0.004	-0.412	Li ₃ Au (<i>Fm-3m</i>)	-0.006
Li ₃ Cu			-0.004	-0.003	Li + LiCu ₃	0.008
Na ₃ Cd			-0.005	-0.059	Na ₃ Cd (<i>P6₃/mmc</i>)	-0.012
Cu ₃ Li			-0.016	-0.040	Cu ₃ Li (<i>I4/mmm</i>)	-0.009
Pd ₃ Hg			-0.018	-0.110	Pd ₃ Hg (<i>Pm-3m</i>)	0.015
Au ₃ Pd			-0.018	-0.071	Au ₃ Pd (<i>Pm-3m</i>)	0.009
Pd ₃ Zn			-0.019	-0.315	Pd ₃ Zn (<i>I4/mmm</i>)	0.006
Ag ₃ Na			-0.020	-0.012	Ag + Ag ₂ Na	0.062
Ag ₃ Li			-0.020	-0.147	Ag ₃ Li (<i>I4/mmm</i>)	-0.009
Pd ₃ Pb			-0.021	-0.249	Pd ₃ Pb (<i>Pm-3m</i>)	0.060
Pd ₃ Bi			-0.022	-0.247	Pd ₃ Bi (<i>Pcmm</i>)	0.022
Cu ₃ Al			-0.022	-0.192	Cu ₃ Al (<i>Pmnm</i>)	-0.002
Cu ₃ Ga			-0.022	-0.113	Cu ₃ Ga (<i>P6₃/mmc</i>)	-0.014
Pd ₃ Au			-0.023	-0.025	Pd ₃ Au (<i>Pm-3m</i>)	0.043
Cu ₃ Be			-0.025	-0.012	Cu + CuBe ₂	0.042
Au ₃ Ag			-0.025	-0.037	Au ₃ Ag (<i>P6₃/mmc</i>)	-0.005
Ag ₃ Mg			-0.025	-0.169	Ag ₃ Mg (<i>P6₃/mmc</i>)	-0.003
Ag ₃ Cd			-0.025	-0.051	Ag ₃ Cd (<i>P6₃/mmc</i>)	-0.002
Cu ₃ Zn			-0.025	-0.072	Cu + Cu ₅ Zn ₈	-0.031
Ag ₃ Pd			-0.026	-0.048	Ag ₃ Pd (<i>I4/mmm</i>)	0.006
Pd ₃ Cd			-0.027	-0.249	Pd ₃ Cd (<i>I4/mmm</i>)	0.011
Ag ₃ Zn			-0.027	-0.028	Ag ₃ Zn (<i>Pm-3m</i>)	0.001
Cu ₃ Mg			-0.028	-0.076	Cu + Cu ₂ Mg	0.032
Pd ₃ Mg			-0.028	-0.469	Pd ₃ Mg (<i>I4/mmm</i>)	0.028
Ag ₃ Au		-0.029	-0.040	Ag + AgAu ₃	-0.029	
Au ₃ Sn		-0.029	-0.072	Au + AuSn	0.019	
Cu ₃ Pd		-0.029	-0.093	Cu ₃ Pd (<i>Pm-3m</i>)	0.016	
Cu ₃ Pt		-0.030	-0.121	Cu ₃ Pt (<i>Pm-3m</i>)	0.017	
Au ₃ Cd		-0.030	-0.130	Au ₃ Cd (<i>P6₃/mmc</i>)	-0.002	
Au ₃ Cu		-0.031	-0.018	Au + AuCu	0.005	
Ni ₃ Be		0.18 (P) 0.24 (M)	-0.032	Ni + NiBe	0.078	
Ni ₃ Zn		0.22 (P) 0.26 (M)	-0.032	Ni + NiZn	0.016	
Au ₃ Zn			-0.033	Au ₃ Zn (<i>I4₁/acd</i>)	0.021	
Cu ₃ Au			-0.034	Cu ₃ Au (<i>Pm-3m</i>)	-0.005	

Table 3 continued

Alloy	This study			Data from MPD ²⁹	
	Magnetic moment (μ_B/atom) ^a	ΔE^{m-p} (eV/atom)	E_f^m (eV/atom)	Reported convex hull ^b	Difference $E_f^m - E_f^{\text{conv}}(\text{MPD})$ (eV/atom)
Sn ₃ Mg		-0.037	-0.013	Sn + SnMg ₂	0.059
Mg ₃ In		-0.037	-0.061	Mg ₃ In (<i>Pm-3m</i>)	0.034
Au ₃ Mn	1.05 (P) 1.05 (M)	-0.044	-0.084	Au ₄ Mn + Au ₂ Mn	0.006
Pd ₃ Cu		-0.045	-0.045	Pd + PdCu ₃	-0.008
Ag ₃ Sc		-0.046	-0.227	Ag ₄ Sc + AgSc	-0.016
Pb ₃ Na		-0.047	-0.093	Pb ₃ Na (<i>Pm-3m</i>)	0.021
Cu ₃ Sc		-0.047	-0.211	Cu ₃ Sc (<i>I4/mmm</i>)	-0.043
Pd ₃ Li		-0.051	-0.230	Pd ₃ Li (<i>Pm-3m</i>)	0.036
Ag ₃ Hf		-0.054	-0.007	Ag + AgHf	0.053
Al ₃ Li		-0.059	-0.052	Al + AlLi	0.038
Pt ₃ Cd		-0.064	-0.114	Pt ₃ Cd (<i>Pm-3m</i>)	0.064
Pt ₃ Zn		-0.065	-0.243	Pt ₃ Zn (<i>Pm-3m</i>)	0.072
Pt ₃ Cu		-0.079	-0.047	Pt ₇ Cu + PtCu	0.060
Ti ₃ In	0.53 (P) 0.00 (M)	-0.086	-0.104	Ti ₃ In (<i>P6₃/mmc</i>)	0.029
Ti ₃ Sn	0.36 (P) 0.00 (M)	-0.089	-0.273	Ti ₃ Sn (<i>P6₃/mmc</i>)	0.022
Ni ₃ Pt	0.48 (P) 0.64 (M)	-0.092	-0.047	Ni ₃ Pt (<i>Pm-3m</i>)	0.025
Ti ₃ Al	0.52 (P) 0.00 (M)	-0.098	-0.252	Ti ₃ Al (<i>P6₃/mmc</i>)	0.026
Ti ₃ Pb	0.35 (P) 0.00 (M)	-0.102	-0.033	Ti ₃ Pb (<i>P6₃/mmc</i>)	0.029
Tc ₃ Be		-0.103	-0.016	Tc + TcBe ₃	0.077
Ti ₃ Hg	0.56 (P) 0.00 (M)	-0.106	-0.016	Ti ₃ Hg (<i>Pm-3n</i>)	0.084
Ti ₃ Zn	0.58 (P) 0.00 (M)	-0.106	-0.088	Ti + Ti ₂ Zn	0.025
Ti ₃ Ga	0.48 (P) 0.00 (M)	-0.112	-0.299	Ti ₃ Ga (<i>P6₃/mmc</i>)	0.021
Zr ₃ Al		-0.130	-0.253	Zr ₃ Al (<i>Pm-3m</i>)	0.046
Ni ₃ Re		-0.139	-0.004	Ni + NiRe ₃	0.033
La ₃ Sn		-0.151	-0.434	La ₃ Sn (<i>Pm-3m</i>)	0.060
Hf ₃ Al		-0.182	-0.207	Hf + Hf ₃ Al ₂	0.001
Al ₃ Co		-0.185	-0.271	Al ₃ Co ₂ + Al ₅ Co ₂	0.143
Y ₃ Bi		-0.199	-0.351	Y + Y ₅ Bi ₃	0.128
Sc ₃ Bi	0.35 (P) 0.00 (M)	-0.214	-0.352	Sc + Sc ₅ Bi ₃	0.044
Zn ₂ YZ					
Zn ₂ LiAg		-0.006	-0.185	Zn ₃ Li + ZnLiAg ₂	-0.011
Zn ₂ CuPt		-0.017	-0.355	Zn ₈ Cu ₅ + Zn ₁₂ Pt ₇ + Cu	-0.012
Zn ₂ NiAu		-0.020	-0.203	ZnNi + ZnAu	0.023
Zn ₂ MnPt	0.92 (P) 0.92 (M)	-0.034	-0.340	Zn ₃ Pt + Zn ₁₂ Pt ₇ + Mn	0.003
Zn ₂ FePt	0.63 (P) 0.69 (M)	-0.037	-0.212	Zn ₃ Pt + Zn ₁₂ Pt ₇ + Fe	0.167
Zn ₂ MgPt		-0.040	-0.492	Zn ₂ Mg + Zn ₃ Pt + Mg ₂ Pt	-0.034
Zn ₂ MgPd		-0.049	-0.417	Zn ₂ Mg + Zn ₃ Pd + MgPd	-0.020
Zn ₂ ScRh		-0.086	-0.569	Zn ₁₁ Rh ₂ + Zn ₁₇ Sc ₃ + ScRh	-0.002
Zn ₂ AlPt		-0.208	-0.468	Zn + Zn ₃ Pt + Al ₃ Pt ₂	0.076
Cu ₂ YZ					
Cu ₂ LiZn		-0.009	-0.120	Cu + LiZn	-0.014
Cu ₂ PdHg		-0.014	-0.019	Cu ₃ Pd + PdHg + Hg	0.083
Cu ₂ NiPd	0.14 (P) 0.14 (M)	-0.023	-0.009	Cu ₃ Pd + Ni + Pd	0.064
Cu ₂ MgAg		-0.026	-0.069	Cu + MgAg ₃ + Cu ₂ Mg	0.059
Cu ₂ ZnAg		-0.030	-0.008	Cu + Ag + Cu ₅ Zn ₈	0.033
Cu ₂ MgAu		-0.032	-0.242	Cu + MgAu	0.063
Cu ₂ NiZn		-0.037	-0.093	Cu + NiZn	0.032
Cu ₂ NiPt	0.15 (P) 0.12 (M)	-0.038	-0.055	Cu ₃ Pt + Ni ₃ Pt	0.061
Cu ₂ MnAu	0.99 (P) 0.99 (M)	-0.040	-0.017	Cu + Mn + MnAu ₂	0.023
Cu ₂ ScAu		-0.043	-0.403	Cu + ScAu	-0.003
Cu ₂ PdIn		-0.043	-0.200	Cu + Pd ₂ In ₃ + Pd ₅ In ₃	0.055
Cu ₂ ZnIr		-0.045	-0.009	Cu + Ir + CuZn ₂ Ir	0.065
Cu ₂ ZnRh		-0.049	-0.124	Cu + ZnRh	0.069

Table 3 continued

Alloy	This study			Data from MPD ²⁹ Reported convex hull ^b	Difference $E_f^m - E_f^{\text{conv}}(\text{MPD})$ (eV/atom)
	Magnetic moment ($\mu\text{B}/\text{atom}$) ^a	ΔE^{m-P} (eV/atom)	E_f^m (eV/atom)		
Cu ₂ MnPd	1.01 (P) 1.05 (M)	-0.051	-0.085	Cu + Mn + CuMnPd ₂	0.027
Cu ₂ ZnPd		-0.052	-0.223	Cu + ZnPd	0.062
Cu ₂ ZnPt		-0.054	-0.252	Cu + ZnPt	0.032
Cu ₂ NbPd		-0.056	-0.089	Cu + Nb + NbPd ₃	0.053
Cu ₂ AlGa		-0.062	-0.109	CuGa ₂ + Cu ₉ Al ₄ + CuAl	0.056
Cu ₂ AlNi		-0.063	-0.283	Cu + AlNi	0.046
Cu ₂ MnPt	1.02 (P) 1.02 (M)	-0.064	-0.163	Cu + MnPt	0.014
Cu ₂ NiGa		-0.065	-0.183	Cu + Ni ₂ Ga ₃ + Ni ₁₃ Ga ₉	0.017
Cu ₂ VPd		-0.072	-0.007	Cu ₃ Pd + V ₃ Pd	0.111
Cu ₂ ZrPd		-0.098	-0.380	Cu ₅ Zr + ZrPd + ZrPd ₃	-0.015
Cu ₂ ScPt		-0.101	-0.593	Cu + ScPt	0.017
Cu ₂ TiPd		-0.103	-0.295	Cu + Cu ₃ Ti + Ti ₂ Pd ₃	-0.012
Cu ₂ VPt		-0.114	-0.165	Cu + VPt	0.114
Cu ₂ NiNb		-0.116	-0.035	Cu + Nb + Ni ₃ Nb	0.061
Cu ₂ Sclr		-0.116	-0.421	Cu + Sclr	0.105
Cu ₂ PdHf		-0.119	-0.403	Cu + Pd ₃ Hf + Cu ₈ Hf ₃	-0.006
Cu ₂ NiTa		-0.133	-0.063	Cu + NiTa ₂	0.081
Cu ₂ ZrRu		-0.205	-0.222	Cu + CuZr	0.108
Ti ₂ YZ					
Ti ₂ AlCd		-0.051	-0.119	Ti ₃ Al + Cd + TiAl	0.121
Ti ₂ RuHg		-0.060	-0.172	Ti ₃ Hg + Hg + TiRu	0.247
Ti ₂ GaIn		-0.076	-0.185	Ti ₂ Ga + In	0.114
Ti ₂ ZnSn		-0.087	-0.206	Ti ₅ Sn ₃ + TiZn ₃	0.087
Ti ₂ Alln		-0.088	-0.176	Ti ₃ In + TiAl + In	0.069
Ti ₂ AlGa		-0.093	-0.359	TiGa + TiAl	0.076
Ti ₂ AlTi		-0.101	-0.035	Ti ₃ Al + Ti + TiAl	0.205
Ti ₂ MgSn		-0.116	-0.138	Ti ₂ Sn + Mg	0.113
Ti ₂ LiSb		-0.120	-0.244	Ti ₃ Sb + Li ₃ Sb	0.219
Ti ₂ PbAl		-0.130	-0.016	TiAl + Ti ₃ Al + Pb	0.224
Ti ₂ AlSn		-0.158	-0.258	Ti ₆ Sn ₅ + TiAl + TiAl ₂	0.129
Ti ₂ MgSb		-0.180	-0.178	Ti ₃ Sb + Ti ₅ Sb ₃ + Mg	0.163
Ti ₂ LiBi		-0.194	-0.060	Ti + Ti ₂ Bi + Li ₃ Bi	0.182

^a Magnetic moments in the ferromagnetic state are shown. P and M denote the magnetic moments of the parent-phase and the martensitic-phase structures, respectively

^b The symbol in the parentheses for the single phase indicates its space-group type

187 surviving alloys are missing in MPD, and therefore the structure on the convex hull in the MPD and that of the present martensitic phase are different for these alloys. The small absolute value of $E_f^m - E_f^{\text{conv}}(\text{MPD})$ less than ~ 0.1 eV/atom may be ascribed to either the difference of the structures or the difference of computational conditions. It may be, however, still reasonable to say that if the $E_f^m - E_f^{\text{conv}}(\text{MPD})$ exceeds ~ 0.1 eV/atom, the alloy may be difficult to be formed or susceptible to the phase separation or transition.

In this study, we considered only the nonmagnetic (NM) and the FM states for each system. If any antiferromagnetism takes place, the energetic stability may be affected. In this study, the 2M martensitic-phase structure (L1₀ in the Strukturbericht symbol and 3R (for B2) and 6R (for D0₃ and L2₁) in the Ramsdell notation) is not considered because it requires tetragonal elongation and is therefore mathematically impossible to simultaneously satisfy $\lambda_2 - 1 = 0$ and $\det(\mathbf{U}) - 1 = 0$. The inverse Heusler structure is not considered as the parent-phase structure because the L2₁ regular Heusler structure is much often found as the parent-phase

structure of SMAs.^{8,56,61} Note that in the cases of $X = \text{Fe, Co, Ni, Ru, Rh, Pd, Os, Ir}$ and Pt in the X_2YZ combinations, it is reported that only 27 combinations among 810 is energetically more stable in the inverse Heusler structure than both in L2₁ and constituting elements.^{62,63} The B19' structure is not considered as the martensitic-phase structure because of the following reasons. Firstly, this structure is expected to give poor structural compatibility with the parent phase. The lattice constants of binary nearly-equiatomic Ti–Ni show poor structural compatibility between the parent B2 and the martensitic B19' structures in experiments.^{64,65} Secondly, the B19' structure has been found in experiments only for Ti–Ni-based alloys.^{23,64,65} Although some Ti–Ni-based ternary alloys with off-stoichiometric composition and doping such as $\text{Ti}_{50.2}\text{Ni}_{34.4}\text{Cu}_{12.3}\text{Pd}_{3.1}$ ⁷ and $\text{Ti}_{54}\text{Ni}_{34}\text{Cu}_{12}$ ⁶⁶ are reported to show low functional fatigue, their martensitic-phase structures are not B19' but B19. It should be also pointed out that the lattice constants and monoclinic angles of the B19' structures have strong dependence on computational conditions⁶⁷ and the constituting chemical elements.²³

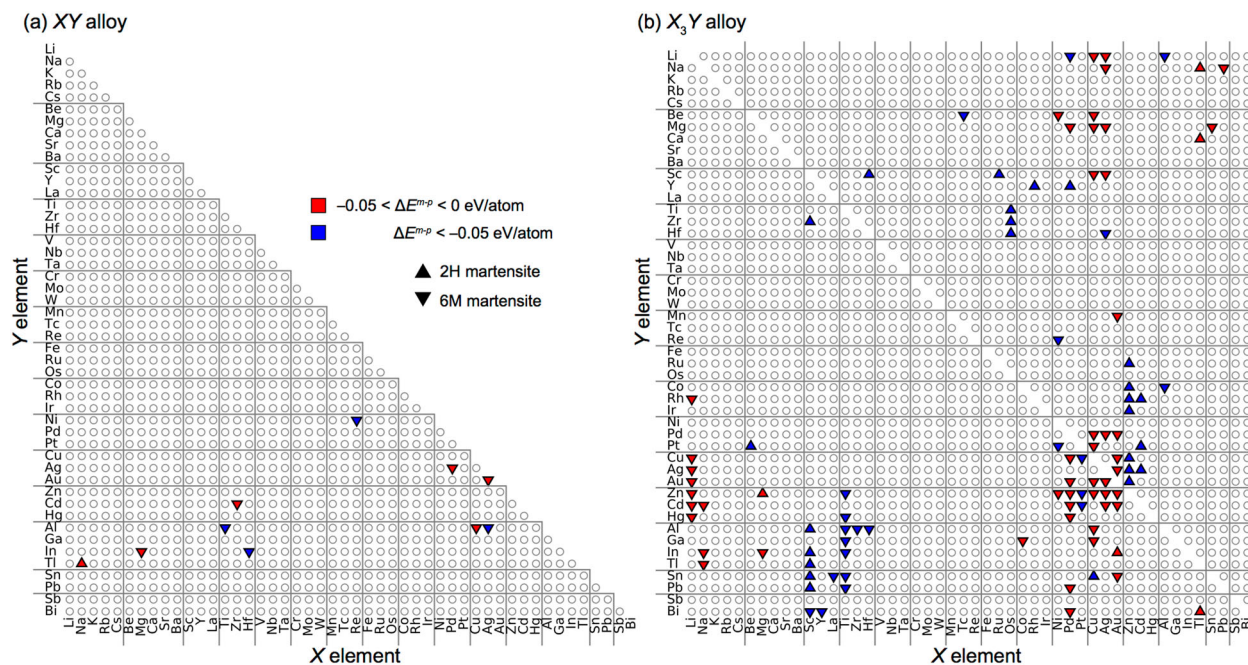


Fig. 9 Combinations of chemical elements in the 111 surviving binary alloys with the composition of **a** XY and **b** X_3Y . Upward and downward triangles classify the type of martensitic-phase structure, and red and blue colors of the triangles classify ΔE^{m-p} . Almost half of the surviving binary alloys (53 out of 111) include some chemical elements in the groups 10–14, while the other 58 surviving binary alloys are found in various combinations of groups

Table 4. Detailed information on the investigated structures as well as on the computational conditions. N denotes the number of atoms in the primitive cell

Phase	Index	Binary XY (B2 parent)	Binary X_3Y (DO_3 parent)	Ternary X_2YZ ($L2_1$ parent)
Parent phase	Space group	$Pm - 3m$	$Fm - 3m$	$Fm - 3m$
	N	$X:1, Y:1$	$X:3, Y:1$	$X:2, Y:1, Z:1$
	k -space sampling ^a	$16 \times 16 \times 16, 24 \times 24 \times 24$ Γ -centered	$16 \times 16 \times 16, 24 \times 24 \times 24$ Γ -centered	$16 \times 16 \times 16, 24 \times 24 \times 24$ Γ -centered
2H martensitic phase	Space group	$Pmma$	$Pnma$	$Pnma$
	N	$X: 2, Y: 2$	$X: 6, Y: 2$	$X: 4, Y: 2, Z: 2$
	k -space sampling ^a	$12 \times 12 \times 12, 16 \times 16 \times 16$ Γ -centered	$12 \times 12 \times 12, 16 \times 16 \times 16$ Γ -centered	$12 \times 12 \times 12, 16 \times 16 \times 16$ Γ -centered
	Supercell size for phonon calculations	$2 \times 4 \times 2$ of primitive cell	$2 \times 2 \times 2$ of primitive cell	$2 \times 2 \times 2$ of primitive cell

^a The finer mesh of the k -space sampling was used for surviving candidates to examine the energy convergence. They are mostly less than 1 meV/atom with the maximum energy difference is only 2 meV/atom

In conclusion, we perform the first-principles-based materials screening to find the intermetallic compounds which possibly cause a martensitic transformation. As the screening conditions, we consider the energetic and dynamical stabilities of the crystal structure in the martensitic phase as well as the structural compatibility of the crystal structures between the parent and the martensitic phases. The B2, DO_3 , and $L2_1$ crystal structures are considered as the parent phase, while the 2H and the 6M structures are considered as the martensitic phase.

We screen 6627 alloys with binary and ternary combinations of chemical elements, resulting in 187 alloys. The surviving alloys are composed of various chemical combinations, indicating that the elements in the wide range in the periodic table should be investigated to discover the alloys with a martensitic transformation. The formation energies of the surviving candidates are further compared with those of the first-principles data in the

MPD to screen out the alloys whose martensitic structure may cause phase separation or transition to other structures.

We also examine the correlation between the martensitic transformation temperature T_c in experiments and the ΔE^{m-p} obtained from the first-principles calculations for the 13 SMAs with nearly stoichiometric composition ratios. Strong correlation is found between the experimental T_c and the computed ΔE^{m-p} . This implies that ΔE^{m-p} can be used to roughly estimate the working temperature range as SMAs.

The findings in this study may also help the discovery of SMAs that overcome the problems of costs, toxicity, and poor functional stability. Although in this study we focus on only the alloys with stoichiometric composition ratios, this study may be a good starting point for investigation also on the alloys with off-stoichiometric composition ratios and provides useful fundamental data. Actually, the off-stoichiometric $Zn_{45}Au_{30}Cu_{25}$ alloy shows

smaller thermal hysteresis and functional fatigue than the stoichiometric Zn_2AuCu alloy,⁸ and hence such composition dependence must be also very interesting.

METHOD

The first-principles calculations are performed by the projector augmented wave (PAW) method^{68,69} implemented in the Vienna ab-initio simulation package (VASP)^{70,71} within the framework of the generalized gradient approximation of Perdew–Burke–Ernzerhof form.⁷² The cutoff energy is set to 400 eV. *k*-space sampling mesh for each investigated structure is summarized in Table 4, and the Methfessel–Paxton scheme⁷³ with a smearing width of 0.4 eV is employed. The volume and shape of the cells and internal atomic coordinates are fully relaxed until residual forces acting on atoms reach below 0.005 eV/Å. The structure optimization is performed for a primitive-cell model to reduce computational costs. Both the NM and the FM states are calculated for each system, and the lower-energy states are investigated in the subsequent materials screening.

The phonon calculations are performed under the harmonic approximation on the lattice Hamiltonian by using the PHONOPY code.^{37,38} To calculate phonon frequencies, in this study we combine the supercell approach and density functional perturbation theory.⁷⁴ Force constants of an alloy are calculated by applying density functional perturbation theory at the Γ point to the supercell model of the alloy. Phonon frequencies are then calculated from the force constants. The supercell size in the phonon calculation for each investigated structure is summarized in Table 4.

We upload the input files of VASP code and optimized crystal structures of surviving compounds as the supplemental information.

Data availability

The authors declare that the data supporting the findings of this study are available within the paper, and the computational conditions for VASP code and crystal structures for surviving 187 alloys are available in its supplementary information files.

ACKNOWLEDGEMENTS

This work was supported by Grant-in-Aid for Scientific Research (A) and Grant-in-Aid for Scientific Research on Innovative Areas “Nano Informatics” (Grant No. 25106005) from the Japan Society for the Promotion of Science (JSPS), and Support program for starting up innovation hub on Materials research by Information Integration” Initiative from Japan Science and Technology Agency. J.L. acknowledges Grant-in-Aid for International Research Fellow of JSPS (Grant No. 2604376) and JSPS fellowships. Y.I. acknowledges Grant-in-Aid for Young Scientist (B) of JSPS (Grant No. 16K18228). Funding by the Ministry of Education, Culture, Sports, Science and Technology (MEXT), Japan, through Elements Strategy Initiative for Structural Materials (ESISM) of Kyoto University, is also gratefully acknowledged.

AUTHOR CONTRIBUTIONS

J.L. and Y.I. proposed the idea for computational works and analyzed theoretical data. J.L. carried out the first principles calculations. I.T. advised the strategy of the research. All authors discussed the results and wrote the manuscript.

ADDITIONAL INFORMATION

Supplementary information accompanies the paper on the *npj Computational Materials* website (<https://doi.org/10.1038/s41524-017-0053-8>).

Competing interests: The authors declare that they have no competing financial interests.

Publisher's note: Springer Nature remains neutral with regard to jurisdictional claims in published maps and institutional affiliations.

REFERENCES

- Jani, J. M., Leary, M., Subic, A. & Gibson, M. A. A review of shape memory alloy research, applications and opportunities. *Mater. Des.* **56**, 1078–1113 (2014).
- Otsuka, K. & Ren, X. Physical metallurgy of Ti–Ni-based shape memory alloys. *Prog. Mater. Sci.* **50**, 511–678 (2005).
- Zhang, Z., James, R. D. & Müller, S. Energy barriers and hysteresis in martensitic phase transformations. *Acta Mater.* **57**, 4332–4352 (2009).
- Biesiekierski, A., Wang, J., Abdel-Hady Gepreel, M. & Wen, C. A new look at biomedical Ti-based shape memory alloys. *Acta Biomater.* **8**, 1661–1669 (2012).
- Dasgupta, R. A look into Cu-based shape memory alloys: present scenario and future prospects. *J. Mater. Res.* **29**, 1681–1698 (2014).
- Huang, W. On the selection of shape memory alloys for actuators. *Mater. Des.* **23**, 11–19 (2002).
- Zarnetta, R. et al. Identification of quaternary shape memory alloys with near-zero thermal hysteresis and unprecedented functional stability. *Adv. Funct. Mater.* **20**, 1917–1923 (2010).
- Song, Y. et al. Enhanced reversibility and unusual microstructure of a phase-transforming material. *Nature* **502**, 85–88 (2013).
- Xue, D. et al. Design of high temperature Ti–Pd–Cr shape memory alloys with small thermal hysteresis. *Sci. Rep.* **6**, 28244 (2016).
- Ma, J., Karaman, I. & Noebe, R. D. High temperature shape memory alloys. *Int. Mater. Rev.* **55**, 257–315 (2013).
- Van Humbeeck, J. High temperature shape memory alloys. *J. Eng. Mater. Technol.* **121**, 98–101 (1999).
- Ullakko, K., Huang, J. K., Kokorin, V. V. & O’Handley, R. C. Magnetically controlled shape memory effect in Ni_2MnGa intermetallics. *Scr. Mater.* **36**, 1133–1138 (1997).
- Chen, X., Srivastava, V., Dabade, V. & James, R. D. Study of the cofactor conditions: conditions of supercompatibility between phases. *J. Mech. Phys. Solids* **61**, 2566–2587 (2013).
- Cui, J. et al. Combinatorial search of thermoelastic shape-memory alloys with extremely small hysteresis width. *Nat. Mater.* **5**, 286–290 (2006).
- Wadood, A. & Yamabe-Mitarai, Y. Recent research and developments related to near-equiatomic titanium–platinum alloys for high-temperature applications. *Platin. Met. Rev.* **58**, 61–67 (2014).
- Atli, K. C. et al. Improvement in the shape memory response of $Ti_{50.5}Ni_{24.5}Pd_{25}$ high-temperature shape memory alloy with scandium microalloying. *Metall. Mater. Trans. A* **41**, 2485–2497 (2010).
- Zarnejad, M. & Liu, Y. Dependence of transformation temperatures of NiTi-based shape-memory alloys on the number and concentration of valence electrons. *Adv. Funct. Mater.* **18**, 2789–2794 (2008).
- Hautier, G. et al. Finding nature’s missing ternary oxide compounds using machine learning and density functional theory. *Chem. Mater.* **22**, 3762–3767 (2010).
- Hinuma, Y. et al. Discovery of earth-abundant nitride semiconductors by computational screening and high-pressure synthesis. *Nat. Comm.* **7**, 11962 (2016).
- Carrete, J. et al. Finding unprecedentedly low-thermal-conductivity half-Heusler semiconductors via high-throughput materials modeling. *Phys. Rev. X* **4**, 011019 (2014).
- Greeley, J. et al. Computational high-throughput screening of electrocatalytic materials for hydrogen evolution. *Nat. Mater.* **5**, 909–913 (2006).
- Belsky, A., Hellenbrandt, M., Karen, V. L. & Luksch, P. New developments in the Inorganic Crystal Structure Database (ICSD): Accessibility in support of materials research and design. *Acta Crystallogr. Sect. B* **58**, 364–369 (2002).
- Huang, X., Ackland, G. J. & Rabe, K. M. Crystal structures and shape-memory behaviour of NiTi. *Nat. Mater.* **2**, 307–311 (2003).
- Huang, X., Rabe, K. M. & Ackland, G. J. First-principles study of the structural energetics of PdTi and PtTi. *Phys. Rev. B* **67**, 024101 (2003).
- Hickel, T. et al. Ab Initio-based prediction of phase diagrams: application to magnetic shape memory alloys. *Adv. Eng. Mater.* **14**, 547–561 (2012).
- Wagner, M. F. X. & Windl, W. Lattice stability, elastic constants and macroscopic moduli of NiTi martensites from first principles. *Acta Mater.* **56**, 6232–6245 (2008).
- Hatcher, N., Kontsevoi, O. Y. & Freeman, A. J. Role of elastic and shear stabilities in the martensitic transformation path of NiTi. *Phys. Rev. B* **80**, 144203 (2009).
- Dutta, B. et al. *Ab initio* prediction of martensitic and intermartensitic phase boundaries in Ni–Mn–Ga. *Phys. Rev. Lett.* **116**, 025503 (2016).
- Jain, A. et al. Commentary: The Materials Project: a materials genome approach to accelerating materials innovation. *Appl. Phys. Lett. Mater.* **1**, 011002 (2013).
- De Graef, M. & McHenry, M. E. *Structure of Materials: An Introduction to Crystallography, Diffraction and Symmetry*, 2nd edn (Cambridge University Press, 2012).
- Otsuka, K., Ohba, T., Tokonami, M. & Wayman, C. M. New description of long period stacking order structures of martensites in β -phase alloys. *Scr. Metall. Mater.* **29**, 1359–1364 (1993).
- Delaey, L. & Chandrasekaran, M. Comments on “New description of long period stacking order structures of martensites in β -Phase alloys” by K. Otsuka, T. Ohba, M. Tokonami and C. M. Wayman. *Scr. Metall. Mater.* **30**, 1605–1610 (1994).
- Nishiyama, Z. *Martensitic Transformation*, 1st edn (Academic, 1978).
- James, R. D. & Hane, K. F. Martensitic transformations and shape-memory materials. *Acta Mater.* **48**, 197–222 (2000).

35. Grimvall, G., Magyari-Köpe, B., Ozoliņš, V. & Persson, K. A. Lattice instabilities in metallic elements. *Rev. Mod. Phys.* **84**, 945–986 (2012).
36. Burgers, W. G. On the process of transition of the cubic-body-centered modification into the hexagonal-close-packed modification of zirconium. *Physica* **1**, 561–586 (1934).
37. Togo, A., Chaput, L., Tanaka, I. & Hug, G. First-principles phonon calculations of thermal expansion in Ti_3SiC_2 , Ti_3AlC_2 , and Ti_3GeC_2 . *Phys. Rev. B* **81**, 174301 (2010).
38. Togo, A., Oba, F. & Tanaka, I. First-principles calculations of the ferroelastic transition between rutile-type and CaCl_2 -type SiO_2 at high pressures. *Phys. Rev. B* **78**, 134106 (2008).
39. James, R. D. & Zhang, Z. A way to Search for Multiferroic Materials with “Unlikely” Combinations of Physical Properties. In *Magnetism and Structure in Functional Materials* (eds. Planes, A., Mañosa, L. & Saxena, A.) (Springer, 2005).
40. Nishijima, M. et al. Accelerated discovery of cathode materials with prolonged cycle life for lithium-ion battery. *Nat. Comm.* **5**, 4553 (2014).
41. Born, M. & Huang, K. *Dynamics Theory of Crystal Lattices* (Oxford University Press, 1954).
42. Nakanishi, N. Lattice softening and the origin of SME. In *Shape Memory Effects in Alloys* (ed. Perkins, J.) (Springer, 1975).
43. Wilkes, K. E. & Liaw, P. K. The fatigue behavior of shape-memory alloys. *JOM* **52**, 45–51 (2000).
44. Craciunescu, C., Kishi, Y., Lograsso, T. A. & Wuttig, M. Martensitic transformation in Co_2NiGa ferromagnetic shape memory alloys. *Scr. Mater.* **47**, 285–288 (2002).
45. Chai, Y. W., Kim, H. Y., Hosoda, H. & Miyazaki, S. Interfacial defects in Ti–Nb shape memory alloys. *Acta Mater.* **56**, 3088–3097 (2008).
46. Padula, S. I. et al. Challenges and progress in the development of high-temperature shape memory alloys based on NiTiX compositions for high-force actuator applications. In *International Conference on Shape Memory and Superelastic Technologies*, 787–801 (eds. Berg, B., Mitchell, M. R. & Proft, J.) (ASM International, Pacific Grove, CA, 2006).
47. Yamabe-Mitarai, Y., Hara, T., Miura, S. & Hosoda, H. Mechanical properties of Ti-50(Pt,Ir) high-temperature shape memory alloys. *Mater. Trans.* **47**, 650–657 (2006).
48. Webster, P. J., Ziebeck, K. R. A., Town, S. L. & Peak, M. S. Magnetic order and phase transformation in Ni_2MnGa . *Philos. Mag. B* **49**, 295–310 (2006).
49. Entel, P. et al. Phase diagrams of conventional and inverse functional magnetic Heusler alloys: New theoretical and experimental investigations. In *Disorder and Strain-induced Complexity in Functional Materials* (eds. Kakeshita, T., Fukuda, T., Saxena, A. & Planes, A.) (Springer, 2013).
50. Hellman, O., Abrikosov, I. A. & Simak, S. I. Lattice dynamics of anharmonic solids from first principles. *Phys. Rev. B* **84**, 180301 (2011).
51. Souvatzis, P., Eriksson, O., Katsnelson, M. I. & Rudin, S. P. Entropy driven stabilization of energetically unstable crystal structures explained from first principles theory. *Phys. Rev. Lett.* **100**, 095901 (2008).
52. Scott, D. W. *Multivariate Density Estimation: Theory, Practice and Visualization*, 1st edn (Wiley, 1992).
53. Tang, W. & Sandström, R. Property database on shape memory alloys for engineering design. In *Computerization and Networking of Materials Databases* (eds. Sturrock, C. P. & Begley, E. F.) (ASTM International, 1995).
54. Schroeder, T. A. & Wayman, C. M. The formation of martensite and the mechanism of the shape memory effect in single crystals of Cu–Zn alloys. *Acta Metall.* **25**, 1375–1391 (1977).
55. Otsuka, K. et al. Superelasticity effects and stress-induced martensitic transformations in CuAlNi alloys. *Acta Metall.* **24**, 207–226 (1976).
56. Kainuma, R., Takahashi, S. & Ishida, K. Thermoelastic martensite and shape memory effect in ductile Cu–Al–Mn alloys. *Metall. Mater. Trans. A* **27**, 2187–2195 (1996).
57. Montecinos, S., Moroni, M. O. & Sepúlveda, A. Superelastic behavior and damping capacity of CuAlBe alloys. *Mater. Sci. Eng. A* **419**, 91–97 (2006).
58. Ogawa, Y., Ando, D., Sutou, Y. & Koike, J. A lightweight shape-memory magnesium alloy. *Science* **353**, 368–370 (2016).
59. Zheng, H. et al. Reversible phase transformations in a shape memory alloy In–Ti nanowires observed by in situ transmission electron microscopy. *Mater. Lett.* **70**, 109–112 (2012).
60. Biggs, T., Cortie, M. B., Witcomb, M. J. & Cornish, L. A. Platinum alloys for shape memory applications. *Platin. Met. Rev.* **47**, 142–156 (2003).
61. Chernenko, V. A., Cesari, E., Kokorin, V. V. & Vitenko, I. N. The development of new ferromagnetic shape memory alloys in Ni–Mn–Ga system. *Scr. Metall. Mater.* **33**, 1239–1244 (1995).
62. Gilleßen, M. & Dronskowski, R. A combinatorial study of full Heusler alloys by first-principles computational methods. *J. Comput. Chem.* **30**, 1290–1299 (2009).
63. Gilleßen, M. & Dronskowski, R. A combinatorial study of inverse Heusler alloys by first-principles computational methods. *J. Comput. Chem.* **31**, 612–619 (2010).
64. Otsuka, K., Sawamura, T. & Shimizu, K. Crystal structure and internal defects of equiatomic TiNi martensite. *Phys. Status Solidi A* **5**, 457–470 (1971).
65. Kudoh, Y., Tokonami, M., Miyazaki, S. & Otsuka, K. Crystal structure of the martensite in Ti-49.2 at.%Ni alloy analyzed by the single crystal X-ray diffraction method. *Acta Metall.* **33**, 2049–2056 (1985).
66. Chluba, C. et al. Ultralow-fatigue shape memory alloy films. *Science* **348**, 1004–1007 (2015).
67. Holec, D., Friák, M., Dlouhý, A. & Neugebauer, J. *Ab initio* study of pressure stabilized NiTi allotropes: Pressure-induced transformations and hysteresis loops. *Phys. Rev. B* **84**, 224119 (2011).
68. Blöchl, P. E. Projector augmented-wave method. *Phys. Rev. B* **50**, 17953–17979 (1994).
69. Kresse, G. & Joubert, D. From ultrasoft pseudopotentials to the projector augmented-wave method. *Phys. Rev. B* **59**, 1758–1775 (1999).
70. Kresse, G. & Furthmüller, J. Efficiency of *ab-initio* total energy calculations for metals and semiconductors using a plane-wave basis set. *Comput. Mater. Sci.* **6**, 15–50 (1996).
71. Kresse, G. & Furthmüller, J. Efficient iterative schemes for *ab initio* total-energy calculations using a plane-wave basis set. *Phys. Rev. B* **54**, 11169–11186 (1996).
72. Perdew, J. P., Burke, K. & Ernzerhof, M. Generalized gradient approximation made simple. *Phys. Rev. Lett.* **77**, 3865–3868 (1996).
73. Methfessel, M. & Paxton, A. T. High-precision sampling for Brillouin-zone integration in metals. *Phys. Rev. B* **40**, 3616–3621 (1989).
74. Baroni, S., Giannozzi, P. & Testa, A. Green’s-function approach to linear response in solids. *Phys. Rev. Lett.* **58**, 1861–1864 (1987).
75. Aroyo, M. I. et al. Brillouin-zone database on the Bilbao Crystallographic Server. *Acta Crystallogr. Sect. A* **70**, 126–137 (2014).



Open Access This article is licensed under a Creative Commons Attribution 4.0 International License, which permits use, sharing, adaptation, distribution and reproduction in any medium or format, as long as you give appropriate credit to the original author(s) and the source, provide a link to the Creative Commons license, and indicate if changes were made. The images or other third party material in this article are included in the article’s Creative Commons license, unless indicated otherwise in a credit line to the material. If material is not included in the article’s Creative Commons license and your intended use is not permitted by statutory regulation or exceeds the permitted use, you will need to obtain permission directly from the copyright holder. To view a copy of this license, visit <http://creativecommons.org/licenses/by/4.0/>.

© The Author(s) 2017